Article

Disentangling the multiorbital contributions of excitons by photoemission exciton tomography

Wiebke Bennecke [1], Andreas Windischbacher [2], David Schmitt[1], Jan Philipp Bange [1], Ralf Hemm[3], Christian S. Kern [2], Gabriele D'Avino [4], Xavier Blase [4], Daniel Steil [1], Sabine Steil[1], Martin Aeschlimann [3], Benjamin Stadtmüller [3], Marcel Reutzel [1], Peter Puschnig [2], G. S. Matthijs Jansen [1] ✉ & Stefan Mathias [1,5] ✉

Excitons are realizations of a correlated many-particle wave function, specifically consisting of electrons and holes in an entangled state. Excitons occur widely in semiconductors and are dominant excitations in semiconducting organic and low-dimensional quantum materials. To efficiently harness the strong optical response and high tuneability of excitons in optoelectronics and in energy-transformation processes, access to the full wavefunction of the entangled state is critical, but has so far not been feasible. Here, we show how time-resolved photoemission momentum microscopy can be used to gain access to the entangled wavefunction and to unravel the exciton's multiorbital electron and hole contributions. For the prototypical organic semiconductor buckminsterfullerene (C_{60}), we exemplify the capabilities of exciton tomography and achieve unprecedented access to key properties of the entangled exciton state including localization, charge-transfer character, and ultrafast exciton formation and relaxation dynamics.

Optical excitations in semiconducting materials deposit energy that can, in the best case, be harnessed in optoelectronic and photovoltaic devices. This potential for energy harvesting holds true over an extremely wide range of semiconducting materials, extending from classical silicon to two-dimensional transition metal dichalcogenides, perovskites and organic semiconductors[1–4]. Hence, major experimental and theoretical research efforts strive to understand such optical excitations.

On the fundamental level, the primary response to the optical excitation is excitonic: Coulomb-correlated electron-hole pairs are created. In the most simple picture, for an organic semiconductor, such an excitation can be understood by the simultaneous creation of an excess electron in the lowest unoccupied molecular orbital (LUMO) and an excess hole in the highest occupied molecular orbital (HOMO). A very fundamental manifestation of the correlated interaction between the electron and hole is the exciton binding energy, which can be observed in optical absorption spectroscopy from the appearance of an absorption feature at one exciton binding energy below the single-particle band gap[5]. Hence, the correlation of the many-body wavefunction serves to reduce the required energy to place a single electron into an excited state.

The concept of excitons does not stop at the lowest HOMO-LUMO excitations, and it provides a natural description of higher excitations as well. This includes transitions that may be described by an electron

[1]I. Physikalisches Institut, Georg-August-Universität Göttingen, Friedrich-Hund-Platz 1, 37077 Göttingen, Germany. [2]Institute of Physics, University of Graz, NAWI Graz, Universitätsplatz 5, 8010 Graz, Austria. [3]Department of Physics and Research Center OPTIMAS, University of Kaiserslautern-Landau, Erwin-Schrödinger-Straße 46, 67663 Kaiserslautern, Germany. [4]Univ. Grenoble Alpes, CNRS, Inst NEEL, F-38042 Grenoble, France. [5]International Center for Advanced Studies of Energy Conversion (ICASEC), University of Göttingen, Göttingen, Germany. ✉e-mail: gsmjansen@uni-goettingen.de; smathias@uni-goettingen.de

in a higher conduction level or a hole in a lower valence level, or the build-up of trions and biexcitons that consist of three or four entangled charged particles[6,7]. Usually, the exciton wavefunction ψ_m is described (in the Tamm-Dancoff approximation) by a superposition of multiple electron-hole pairs[8]:

$$\psi_m(\boldsymbol{r}_h, \boldsymbol{r}_e) = \sum_{v,c} X_{vc}^{(m)} \phi_v^*(\boldsymbol{r}_h) \chi_c(\boldsymbol{r}_e). \tag{1}$$

Here ϕ_v and χ_c are the vth valence and c^{th} conduction states of the ground-state system, respectively. The coefficients $X_{vc}^{(m)}$ can create an entangled state where the electron and hole coordinates ($\boldsymbol{r}_e$ and $\boldsymbol{r}_h$) cannot be considered independently (Fig. 1). Access to this orbital picture of the excitonic wavefunction is highly valuable[9], because imaging of the full entangled state would give direct access to exciton properties such as localization and charge-transfer character. Indeed, this information is particularly critical in the case of organic semiconductors, where it is well-known that such multiorbital correlated quasiparticles dominate the energy landscape[10,11]. However, it must be emphasized that conventional optical spectroscopy methods, including absorption and fluorescence spectroscopy, only provide access to the exciton energy Ω_m, and do not provide any information about the multiorbital contributions ($\phi_v^*\chi_c$) of the exciton (see Fig. 1a, b).

For single-particle molecular orbitals in organic semiconductors, an imaging of the wavefunction is possible through photoemission orbital tomography[12,13]. In the last years, this technique was increasingly used to study light-induced dynamics in organic semiconductors[14,15] and 2D quantum materials[16–18], which exemplified the tremendous capabilities of this technique when applied to excitonic states. However, the full potential of photoemission exciton tomography was only recently indicated in a theoretical study by Kern et al., and promises to unravel the entangled single-particle orbital contributions and real-space properties of the excitons[19]. In this article, we experimentally introduce photoemission exciton tomography (Fig. 1c) and use it for the first time to characterize the correlated excitonic electron-hole state in an organic semiconductor. Specifically, we find that the detected photoelectron kinetic energy provides a sensitive probe of the hole component of the exciton, and furthermore that the photoelectron momentum map probes the spatial properties of the electron component.

Results and discussion

The exciton spectrum of C_{60}

In order to introduce the photoemission exciton tomography approach, we select $(C_{60} - I_h)$[5,6]fullerene (C_{60}) as an ideal, widely used[20–22] and prototypical example. In particular, C_{60} shows a series of optical absorption features in multilayer and other aggregated structures[23], where different spectroscopy studies have indicated that these optical transitions correspond to the formation of excitons with differing charge-transfer character[24–28]. Although these indirect results are supported by time-dependent density functional theory calculations[29–31], quantitative access to the multiorbital wavefunction contributions (see Eq. (1) and Fig. 1) has so far not been feasible. Thus, the C_{60} organic semiconductor is an ideal platform to showcase the capabilities of photoemission exciton tomography.

In theory, we obtain the exciton spectrum by employing the many-body framework of GW and Bethe-Salpeter-Equation (GW+BSE) calculations on top of a hybrid-functional density functional theory (DFT) ground state calculation (Fig. 2a, see Methods)[8,32]. We find that the C_{60} crystal (Fig. 2a) can be accurately described using two symmetry-inequivalent C_{60} dimers (see Supplementary Information, Supplementary Figs. S1, S4 and S5 for an experimental determination of the crystal structure and a convergence analysis of the dimer model). The calculated single-particle energy levels are shown in Fig. 2b, where we group the electron removal and electron addition energies into four bands, denoted according to the parent orbitals of the gas-phase C_{60} molecule. Building upon the GW single-particle energies (Fig. 2b), we solve the Bethe-Salpeter equation and compute the energies Ω_m of all correlated electron-hole pairs (excitons), which results in the absorption spectrum shown in the bottom panel of Fig. 2c. Furthermore, we obtain the weights $X_{vc}^{(m)}$ on the specific electron-hole pairs that build-up the mth exciton state by Eq. (1). This provides a full description of the multiorbital entangled excitons, and thereby contains the full spatial properties of each exciton.

To gain more insight into the character of the excitons ψ_m, we qualitatively classify them according to the most dominant orbital contributions that are involved in the transitions. This is visualized in the four sub-panels above the absorption spectrum in Fig. 2c. For a given exciton energy Ω_m, the black bars in each sub-panel show the partial contribution $|X_{vc}^{(m)}|^2$ of characteristic electron-hole transitions $\phi_v\chi_c$ to a given exciton ψ_m. Looking at individual sub-panels, we see
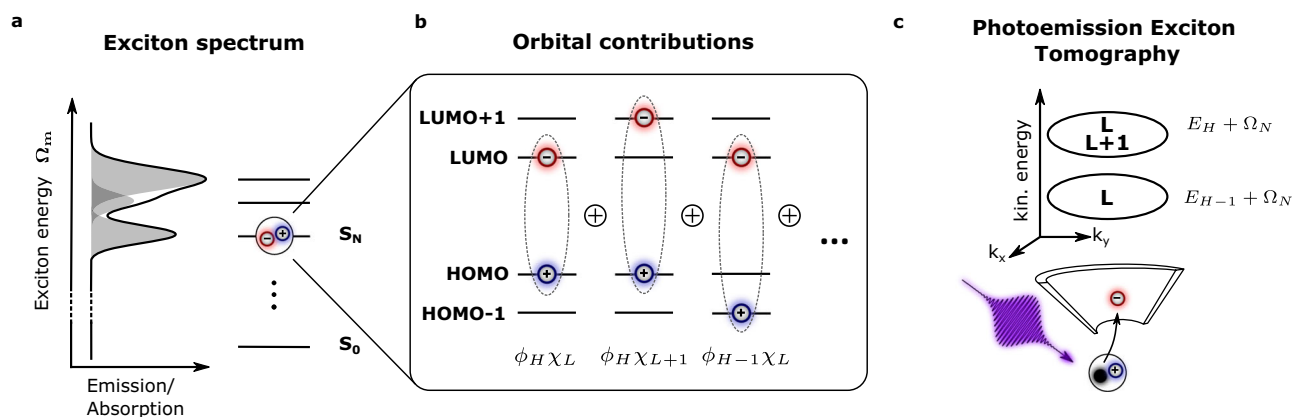

Fig. 1 | The optical response of many semiconducting materials is described by the excitation of excitons. a In the exciton picture, each excited state is described by an exciton energy Ω_m, which (for bright excitons) can be measured by optical spectroscopy. **b** At the orbital level, however, each exciton is built up by an entangled sum of electron-hole pairs $\phi_v\chi_c$ (see Eq. (1)). In this description, the sum of orbital contributions provides complete access to the spatial properties of the exciton. **c** In photoemission exciton tomography, a high-energy photon photoemits the electron and thereby breaks up the exciton. The single-particle electron orbitals (here LUMO (L) and LUMO+1 (L+1)) contributing to the exciton are imprinted on the photoelectron momentum distribution, while the kinetic energy distribution probes the contributing hole orbitals by measuring the hole binding energy E_H (see Eq. (2)). A full momentum- and energy-resolved measurement of the photoelectron spectrum therefore provides an ideal starting point for a comparison to ab-initio calculations of the excitonic wavefunction, and thereby provides access to the spatial properties of the exciton.
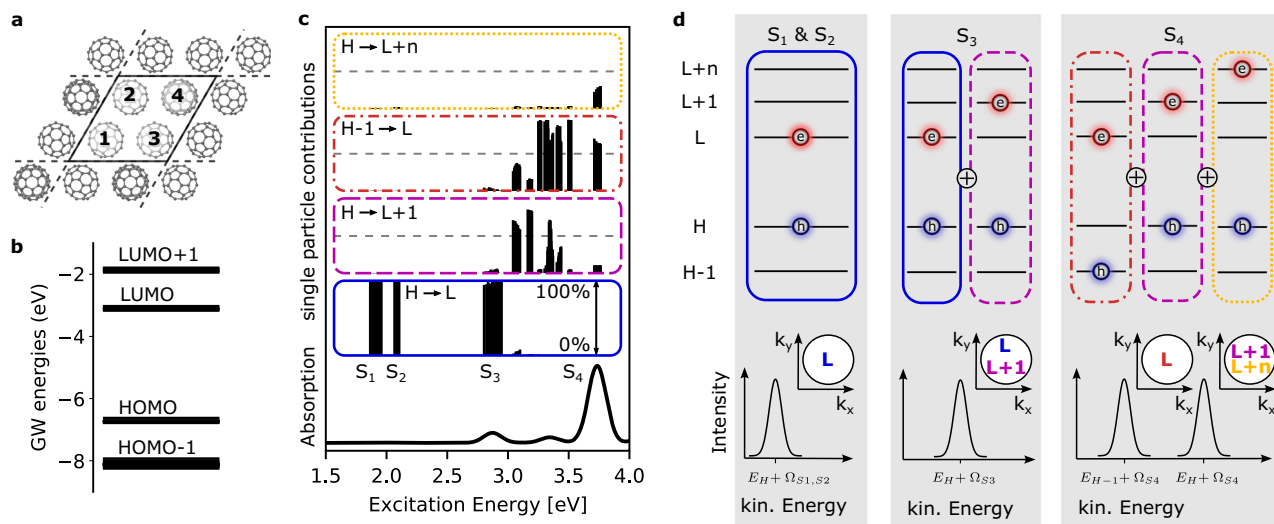
Fig. 2 | Ab-initio calculation of the electronic structure and exciton spectrum of C$_{60}$ dimers in a crystalline multilayer sample. a The unit cell for a monolayer of C$_{60}$, for which *GW*+BSE calculations for the dimers 1-2 and 3-4 were performed. **b** Electron addition/removal single-particle energies as retrieved from the self-consistent *GW* calculation. These energies directly provide ε_v in Eq. (2). The HOMO-LUMO manifolds consist of 18, 10, 6, and 6 energy levels per dimer, respectively, originating from the $g_g + h_g$, h_u, t_{1u}, and t_{1g} irreducible representations of the gas phase C$_{60}$ orbitals[56]. **c** Results of the full *GW*+BSE calculation in accordance with

ref. 23, showing as a function of the exciton energy Ω from bottom to top: the calculated optical absorption, the exciton band assignment S$_1$ - S$_4$, and the relative contributions to the exciton wavefunctions of different electron-hole pair excitations $\phi_v \chi_c$. Full details on the calculations are given in the Methods section. **d** Sketch of the composition of the exciton wavefunction of the S$_1$ - S$_4$ bands and their expected photoemission signatures based on Eq. (2). In order to visualize the contributing orbitals, blue holes and red electrons are assigned to the single-particle states as shown in (**b**).

that not only the excitons are commonly composed of multiple characteristic electron-hole transitions, but also that single electron-hole transitions can belong to different excitons ψ_m that have very different exciton energies Ω_m. For example, the blue panel in Fig. 2c shows the contributions of HOMO → LUMO (abbreviated H → L) transitions as a function of exciton energy Ω_m, and we see that these transitions contribute to excitons that are spread in energy over a scale of more than 1 eV (from $\Omega_m \approx 1.7$ eV–3 eV). This spread of H → L contributions (and also H − n → L+m contributions) is caused by the fact that there are already many orbital energies per dimer (see Fig. 2b) which combine to form excitons with different degrees of localization and delocalization of the electrons and holes on one or more molecules.

We now focus on four exciton bands of the C$_{60}$ film, denoted as S$_1$ - S$_4$, which are centered around Ω_{S1}, Ω_{S2}, Ω_{S3} and Ω_{S4} at 1.9, 2.1, 2.8 and 3.6 eV, respectively. Notably, S$_2$ and S$_3$ were previously found to have charge-transfer character[24,25], while S$_4$ stands out due to a fundamentally different wavefunction composition. It is important to emphasize that each exciton band S$_1$ - S$_4$ arises from many individual excitons ψ_m with similar exciton energies Ω_m within the exciton band. From Fig. 2c, we see that the S$_1$ and S$_2$ exciton bands are made up of excitons ψ_m that are almost exclusively composed of transitions from H → L. On the other hand, S$_3$ shows in addition to H → L also weak contributions from H → L+1 transitions (pink-dashed panel). The S$_4$ exciton band can be characterized as arising from H → L+1 (pink-dashed panel) and H − 1 → L (orange-dash-dotted panel) as well as transitions from the HOMO to several higher lying orbitals denoted as H → L+n (yellow-dotted panel). Note that the inclusion of electron-hole correlations has important consequences on the composition of the exciton wave function ψ_m[33,34]. Specifically, S$_3$ is not only composed of H → L transitions but exhibits also an admixture of H → L+1 transitions despite the calculated ≈1 eV energy separation of quasiparticle LUMO and LUMO+1 levels.

Photoemission signature of multiorbital entangled excitons

In the following, we investigate whether these theoretically predicted multiorbital characteristics of the excitons can also be probed

experimentally. Therefore, we take the exciton of Eq. (1) as the initial state and apply the common plane-wave final state approximation of photoemission orbital tomography[19]. The photoemission intensity of the exciton ψ_m is formulated as

$$I_m(E_{\mathrm{kin}}, \boldsymbol{k}) \propto |\boldsymbol{A}\boldsymbol{k}|^2 \sum_v \left| \sum_c X_{vc}^{(m)} \mathcal{F}[\chi_c](\boldsymbol{k}) \right|^2 \times \delta(h\nu - E_{\mathrm{kin}} - \varepsilon_v + \Omega_m). \quad (2)$$

Here $\boldsymbol{A}$ is the vector potential of the incident light field, $\mathcal{F}$ the Fourier transform, $\boldsymbol{k}$ the photoelectron momentum, $h\nu$ the probe photon energy, ε_v the vth ionization potential, Ω_m the exciton energy, and E_{kin} the energy of the photoemitted electron. Note that ε_v directly indicates the final-state energy of the left-behind hole. In the context of our present study, delving into Eq. (2) leads to two striking consequences that allow us to disentangle the electron and hole contributions of the exciton, which we discuss in the following.

First, we will discuss the importance of the hole contribution based on the consequences of the multiorbital entangled character for the photoelectron spectrum for the four different exciton bands in C$_{60}$. In Fig. 2d, we sketch the typical single-particle energy level diagrams for the HOMO and LUMO states and indicate the contributing orbitals to the two-particle exciton state by blue holes and red electrons in these states, respectively. For the S$_1$ exciton band (left panel), we already found that the main orbital contributions to the band are of H → L character (Fig. 2d, left, and see Fig. 2c, blue panel). To determine the kinetic energy of the photoelectrons originating from the exciton, we have to consider the correlated nature of the electron-hole pair. The energy conservation expressed by the delta function in Eq. (2) (see also refs. 35–37) requires that the kinetic energy of the photoelectron depends on the ionization energy of the involved HOMO hole state $\varepsilon_v = \varepsilon_H$ and the correlated electron-hole pair energy $\Omega \approx \Omega_{S1}$. Therefore, we expect to measure a single photoelectron peak, as shown in the lower part of the left panel of Fig. 2d. In the case of the S$_2$ exciton the situation is similar, since the main orbital contributions are also of H → L character. However, since the S$_2$ exciton band has a higher
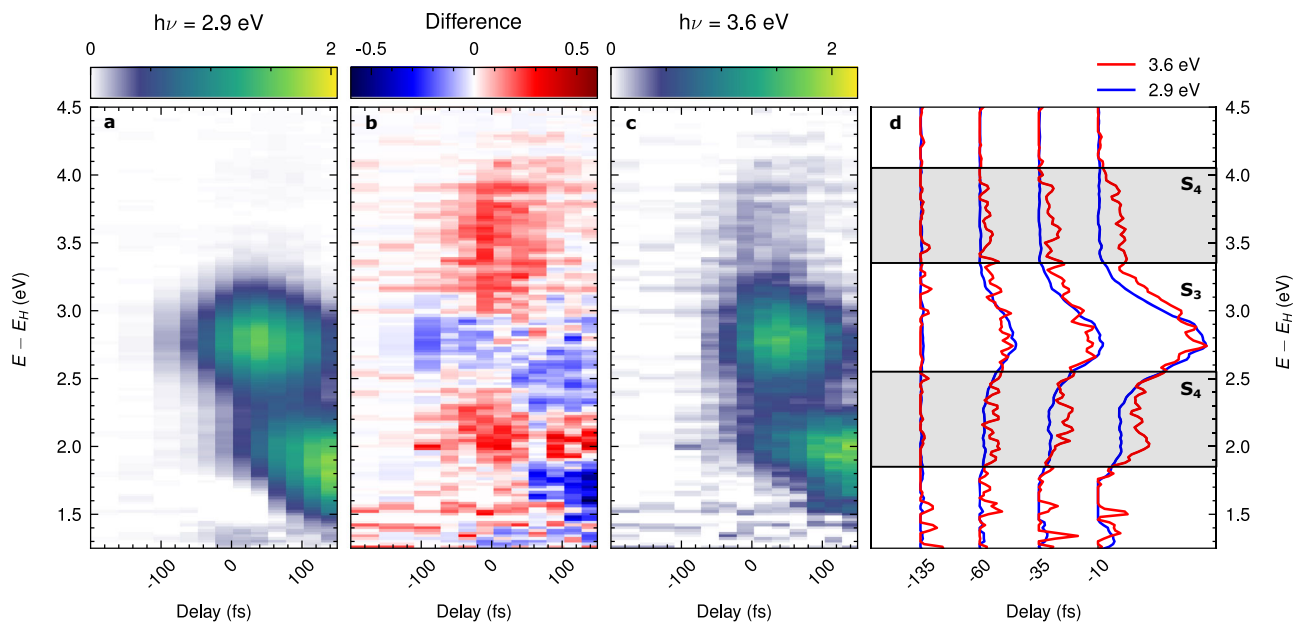
Fig. 3 | Comparison of the exciton dynamics of multilayer C_{60} for hv = 2.9 eV excitation and hv = 3.6 eV excitation. a, **c** show the time-resolved photoelectron spectra, both normalized and shifted in time to match the intensity of the S_3 signals (see Methods for full details on the data analysis). As can be seen in the difference **b** for hv = 3.6 eV pump we observe an enhancement of the photoemission yield around $E - E_H \approx 3.6$ eV as well as around $E - E_H \approx 2.2$ eV. We attribute this signal to the S_4 exciton band, which has hole contributions stemming from both the HOMO and the HOMO-1. To further quantify the signal of the S_4 exciton, **d** shows energy distribution curves for both measurements at early delays, showing the enhancement in the hv = 3.6 eV measurement.

energy Ω_{S2}, the photoelectron peak is also located at a higher kinetic energy with respect to the S_1 peak.

In the case of the S_3 exciton band, we find that in contrast to the S_1 and S_2 excitons not only H → L, but also H → L+1 transitions contribute (Fig. 2d, middle panel, and see Fig. 2c, blue and pink-dashed panels, respectively). However, we still expect a single peak in the photoemission, because the same hole states are involved for both transitions (i.e., same $\varepsilon_v = \varepsilon_H$ in the sum in Eq. (2)), and all orbital contributions have the same exciton energy $\approx \Omega_{S3}$, even though transitions with electrons in energetically very different single-particle LUMO and LUMO+1 states contribute. With other words, and somewhat counter-intuitively, the single-particle energies of the electron orbitals (the LUMOs) contributing to the exciton do not enter the energy conservation term in Eq. (2), and thus do not affect the kinetic energy observed in the experiment.

Finally, for the S_4 exciton band at $\Omega_{S4} = 3.6$ eV, we find three major contributions (Fig. 2d, right panel), where not only the electrons but also the holes are distributed over two energetically different levels, namely the HOMO (see pink-dashed and yellow-dotted panels in Fig. 2c, d) and the HOMO-1 (see orange-dash-dotted panels in Fig. 2c, d). Thus, there are two different final states available for the hole, each with a different binding energy. Consequently, the photoemission spectrum of S_4 is expected to exhibit a double-peak structure with intensity appearing ≈ 3.6 eV above the HOMO kinetic energy E_H, and ≈ 3.6 eV above the HOMO-1 kinetic energy E_{H-1}, as illustrated in the right-most panel of Fig. 2d. Relating this specifically to the single-particle picture of our *GW* calculations, the two peaks are predicted to have a separation of $\varepsilon_{H-1} - \varepsilon_H = (8.1 - 6.7)$ eV = 1.4 eV. In summary, the photoelectron energy distribution provides access to the multiorbital character of the exciton, because different hole states that contribute to the exciton induce a multipeak structure in the spectrum.

The second consequence of Eq. (2) concerns the electron contribution, which modifies the photoemission momentum distribution. In analogy to conventional photoemission orbital tomography, Eq. (2) provides the theoretical framework for interpreting time- and

momentum-resolved data from excitons. Ground state momentum maps can be easily understood in terms of the Fourier transform $\mathcal{F}$ of single-particle orbitals[12]. A naive extension to excitons might imply an incoherent, weighted sum of all conduction orbitals χ_c contributing to the exciton wavefunction. However, as Eq. (2) shows, such a simple picture proves insufficient. Instead, the momentum pattern of the exciton wavefunction is related to a coherent superposition of the electron orbitals χ_c weighted by the electron-hole coupling coefficients $X_{vc}^{(m)}$. The implications of this finding are sketched in the k_x-k_y plots in Fig. 2d and are most obvious for the S_3 band. Here, the exciton is composed of transitions with a common hole position, i.e., H → L and H → L+1, leading to a coherent superposition of all 12 electron orbitals from the LUMO and LUMO+1 in the momentum distribution. In summary, multiple hole contributions can be identified in a multi-peak structure in the photoemission spectrum, and multiple electron contributions will result in a coherent sum of the electron orbitals that can be identified in the corresponding energy-momentum patterns of time-resolved data.

Disentangling multiorbital contributions experimentally

These very strong predictions about multi-peaked photoemission spectra due to multiorbital entangled excitons can be directly verified in an experiment on C_{60} by comparing spectra for resonant excitation of either the S_3 or the S_4 excitons (see Fig. 2). We employ our recently developed setup for photoelectron momentum microscopy[38,39] and use ultrashort laser pulses to optically excite the S_3 and the S_4 bright excitons in C_{60} thin films that were deposited on Cu(111) (measurement temperature T ≈ 80 K, p-polarized excitation; see Methods). The corresponding time-resolved photoelectron spectra of the electrons that were initially part of the bound electron-hole pairs are shown in Fig. 3a and c, respectively. Starting from the excitation of the S_3 exciton band with hv = 2.9 eV photon energy (which is sufficiently resonant to excite the manifold of exciton states that make up the S_3 band around $\Omega_{S3} = 2.8$ eV), we can clearly identify the direct excitation (at 0 fs delay) of the exciton S_3 feature at an energy of $E \approx 2.8$ eV above the kinetic energy E_H of the HOMO level. Shortly after the excitation, additional

photoemission intensity builds up at $E - E_H \approx 2.0$ eV and ≈ 1.7 eV, which is known to be caused by relaxation to the S_2 and S_1 dark exciton states[25] and is in good agreement with the theoretically predicted energies of $E - E_H \approx 2.1$ eV and ≈ 1.9 eV (see Fig. 2c, blue panel).

Changing now the pump photon energy to hv = 3.6 eV for direct excitation of the S_4 exciton band (Fig. 3c), two distinct peaks at ≈ 3.6 eV above the HOMO and ≈ 3.6 eV above the HOMO-1 are expected from theory. While photoemission intensity at $E - E_H \approx 3.6$ eV above the HOMO level is readily visible in Fig. 3c, the second feature at 3.6 eV above the HOMO-1 is expected at $E - E_H \approx 2.2$ eV above the HOMO level (corresponding to $E - E_{H-1} \approx 3.6$ eV) and thus almost degenerate with the aforementioned S_2 dark exciton band at about $E - E_H \approx 2.0$ eV, which appears after the optical excitation due to relaxation processes. We note that a fast relaxation to the band of exciton states between 3.0 and 3.5 eV (see Fig. 2c) is also possible and may contribute to the observed signal. However, these excitons also have contributions from the HOMO and HOMO-1 and are thus also predicted to lead to two distinct peaks at somewhat lower ≈ 3.4 eV above the HOMO and HOMO-1, thereby also confirming our expectations from theory. In any case, we therefore need to pinpoint the second $H - 1 \rightarrow L$ lower energy contribution from either the S_4 or the exciton band around 3.0–3.5 eV, and we do this by analyzing our data at the earliest time of excitation, i.e. before relaxation to the S_2 dark exciton band occurs, which is degenerate at this photoelectron energy of ≈ 2.2 eV. Indeed, we find that a closer look around 0 fs delay shows additional photoemission intensity at this particular energy. Using a difference map (Fig. 3b) and direct comparisons of energy-distribution-curves at selected time-steps (Fig. 3d), we clearly find a double-peak structure corresponding to the energy difference of ≈ 1.4 eV of the HOMO and HOMO-1 levels. Thereby, we have shown that photoelectron spectroscopy, in contrast to other techniques (e.g., absorption spectroscopy), is indeed able to disentangle different orbital contributions of the excitons. In this way, we have validated the theoretically predicted multi-peak structure of the multiorbital exciton state that is implied by Eq. (2). We also see that the photoelectron energies in the spectrum turn out to be sensitive probes of the corresponding hole contributions of the correlated exciton states.

We note that the signature of the S_3 excitons, even if not directly excited with the light pulse in this measurement, is still visible and moreover with significantly higher intensity than the multiorbital signals of the resonantly excited S_4 exciton band. The explanation for this effect is two-fold: first, the time-resolved signature suggests a very fast relaxation of the S_4 excitons to the S_3, with relaxation times well below 50 fs (see Supplementary Fig. S3). Second, a calculation following Eq. (2) predicts an about threefold reduced photoemission matrix element for the S_4 compared to the S_3 band, explaining the overall weaker signal.

Time-resolved photoemission exciton tomography

In the full time-resolved photoemission experiment, by following the time-evolution of all electrons that were initially part of bound electron-hole pairs, one can observe how the optically-excited states relax to energetically lower-lying dark exciton states[17,18,24,25,35,40,41] (Supplementary Fig. S3) with the expected different localization and charge-transfer character. Importantly, the photoemission momentum microscope collects full time- and momentum-resolved data (i.e., 4D data set with time, energy and 2D momentum resolution), which we now show is ideal to access the spatial properties of the entangled multiorbital contributions.

We once again excite the S_3 exciton band in the C_{60} film with hv = 2.9 eV pump energy, and collect the momentum fingerprints of the directly excited S_3 excitons around 0 fs and the subsequently built-up dark S_2 and S_1 excitons that appear in the exciton relaxation cascade in the C_{60} film (see Fig. 4a, where the momentum maps of the lowest energy S_1 exciton band, the S_2 and the highest energy S_3 exciton band

are plotted from left to right; see Supplementary Fig. S3 for time-resolved traces of the exciton formation and relaxation dynamics). We note that the collection of the S_1, S_2, and S_3 momentum maps already required integration times of up to 70 hours and a summation of the data over all measured time-steps from -200 fs–15 ps (see Methods), so that a measurement of the comparatively low-intensity S_4 feature when excited with hv = 3.6 eV has not yet proved feasible. For the interpretation of the collected momentum maps from the S_1, S_2, and S_3 excitons, we also calculate the expected momentum fingerprints for the wavefunctions obtained from the GW+BSE calculation for both dimers, each rotated to all occurring orientations in the crystal. Finally, for the theoretical momentum maps, we sum up the photoelectron intensities of each electron-hole transition in an energy range of 200 meV centered on the exciton band. The results are shown in Fig. 4c below the experimental data for direct comparison.

First, recapitulating from Fig. 2c that the S_1 and the S_2 exciton bands are both only comprised of $H \rightarrow L$ transitions, we expect nearly identical momentum maps (but at different energies). Indeed, the experimental S_1 and S_2 momentum maps are largely similar (Fig. 4a), showing six lobes centered at $k_{\parallel} \approx 1.25$ Å^{-1}. These six-lobe features, as well as the energy splitting between S_1 and S_2 (see Fig. 2c), are accurately reproduced by the GW+BSE prediction (Fig. 4b). Furthermore, the GW+BSE calculation also shows identical momentum maps for S_1 and S_2 confirming that the result of the coherent sum over all $H \rightarrow L$ transitions (Eq. (2)) is similar, and also indicates that the S_1 and the S_2 exhibit a similar spatial structure of the exciton wavefunction. This is in contrast to a naive application of static photoemission orbital tomography to the unoccupied orbitals of the DFT ground state of C_{60}, which does indicate a similar momentum map for the LUMO, but cannot explain a kinetic energy difference in the photoemission signal, nor give any indication of differences in the corresponding exciton wavefunctions. With this agreement between experiment and theory, we now extract the spatial properties of the GW+BSE exciton wavefunctions. To visualize the degree of charge-transfer of these two-particle exciton wavefunctions $\psi_m(\mathbf{r}_h, \mathbf{r}_e)$, we integrate the electron probability density over all possible hole positions $\mathbf{r}_h$, considering only hole positions at one of the C_{60} molecules in the dimer. This effectively fixes the hole contribution to a particular C_{60} molecule (blue circles in Fig. 4c indicate the boundary of considered hole positions around one molecule, hole distribution not shown), and provides a probability density for the electronic part of the exciton wavefunction in the dimer, which we visualize by a yellow isosurface (see Fig. 4c). For the S_1 and S_2, when the hole position is restricted to one molecule of the dimer, the electronic part of the exciton wavefunction is localized at the same molecule of the dimer. Our calculations thus suggest that the S_1 and S_2 excitons are of Frenkel-like nature. Their energy difference originates from different excitation symmetries possible for the $H \rightarrow L$ transition (namely t_{1g}, t_{2g}, and g_g for the S_1 and h_g for the S_2)[31].

Compared to the S_1 and S_2 exciton bands, the S_3 band is not only composed of $H \rightarrow L$ transitions, but also has a minor contribution of $H \rightarrow L+1$ transitions (see Fig. 2c). We therefore expect that the S_3 momentum map cannot be identical to the S_1 and S_2 momentum maps, but must show a signature of the $H \rightarrow L+1$ contribution in addition to a possibly different coherent sum of all involved $H \rightarrow L$ transitions. Indeed, a closer look at the experimental data shows a more spoke-like structure for S_3, which is marked with red arrows for three of the six spokes in the raw data as a guide to the eye (Fig. 4a, top right). An analysis over all different orientations, i.e. effectively symmetrizing the data, makes the spoke-structure even better visible (Fig. 4a, bottom right, and Supplementary Fig. S6 for momentum lineouts). Hence, our experimental data clearly confirms the different character of the S_3 exciton band in comparison to S_1 and S_2. Looking at the theoretical data, we also find differences between the nearly identical S_1 and S_2 momentum maps (Fig. 4b) in comparison to the S_3 momentum map. Once again, the differences are marked with red arrows as a guide to
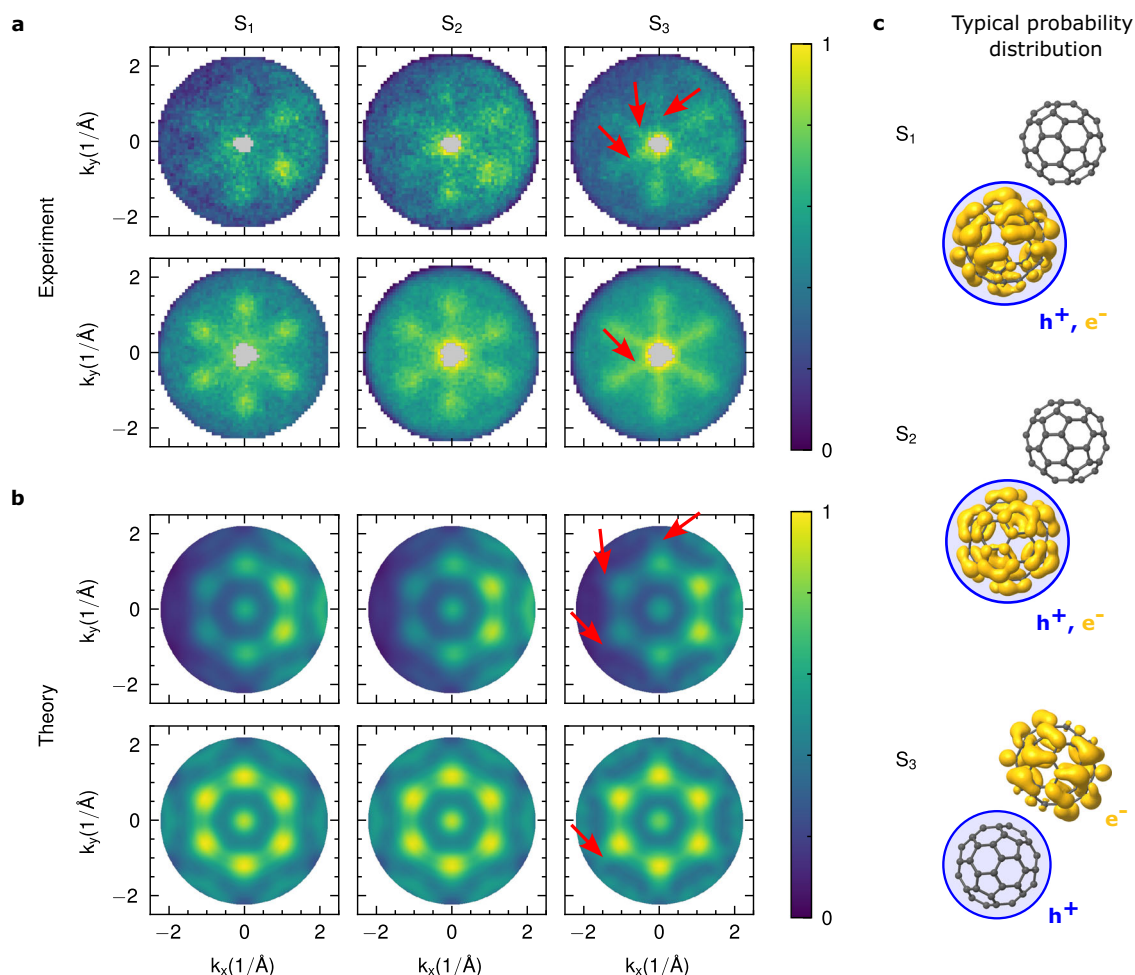
Fig. 4 | Photoelectron momentum distribution and exciton real space probability distribution of the three exciton bands observed in C_{60}. **a** Comparison of the experimental momentum maps acquired for the S_1, S_2 and S_3, with the **b** predicted momentum maps retrieved from GW+BSE. The top rows show the raw data and the bottom rows 6-fold symmetrized data, respectively. Note that the

center of the experimental maps could not be analyzed due to a space-charge-induced background signal in this region (gray area, see Methods). **c** Isosurfaces of the integrated electron probability density (yellow) within the 1-2 dimer for fixed hole positions on the bottom-left molecule (blue circle) of the dimer for the S_1, the S_2, and the S_3 exciton bands.

the eye (Fig. 4b, top right and bottom right, respectively; lineout analysis in Fig. S6). However, we also find that the experimentally observed spoke-like pattern for S_3 is different to the S_3 momentum structure calculated using the dimer model. An indication towards the cause of this discrepancy is found by considering the electron-hole separation of the excitons making up the S_3 band. Here, we find that the positions of the electron and the hole contributions are strongly anticorrelated (Fig. 4c), with the electron confined to the neighboring molecule of the dimer. In fact, the mean electron-hole separation is as large as 7.6 Å, which is close to the core-to-core distance of the C_{60} molecules. Although these theoretical results confirm the previously-reported charge-transfer nature of the S_3 excitons[24,25], they also reflect the limitations of the C_{60} dimer approach. Indeed, the dimer represents the minimal model to account for an intermolecular exciton delocalization effect, but it cannot fully account for dispersion effects[42] (see Supplementary Fig. S1), which are required for a quantitative comparison with experimental data. Besides the discrepancy in the S_3 momentum map, this could also be an explanation why the S_2 in the present work is of Frenkel-like nature, but could have charge-transfer character according to previous studies[24,25]. However, future developments will certainly allow scaling up of the cluster size in the calculation and to include periodic boundary conditions, so that exciton wavefunctions with larger electron-hole separation can be accurately described. Most

importantly, we find that the present dimer GW+BSE calculations are clearly suited to elucidate the multiorbital character of the excitons, which is an indispensable prerequisite for the correct interpretation of time- and momentum-resolved data of excitons in organic semiconductors.

In conclusion, we introduced photoemission exciton tomography to unravel the multiorbital electron and hole contributions of entangled excitonic states. In a case study on C_{60}, we show how to connect time- and angle-resolved photoelectron spectroscopy data to the wavefunction of fully-interacting exciton states. For the hole component of the exciton, the spectral position of the hole is reflected in the photoelectron kinetic energy distribution, leading to the appearance of multiple peaks in the photoelectron spectrum for a multiorbital exciton. At the same time, the momentum fingerprint provides access to the electron states that make up the exciton. Applying this analysis to the observed exciton photoelectron spectrum of C_{60}, we were able to access important key properties including different orbital contributions, the wavefunction localization, and the charge-transfer character. We anticipate that photoemission exciton tomography will contribute to the understanding of exciton dynamics and the harnessing of such particles not only in organic semiconductors, but in general to advanced optoelectronic and photovoltaic devices.

Methods

Femtosecond momentum microscopy of C_{60}/Cu(111)

We apply full multidimensional time- and angle-resolved photoelectron spectroscopy (tr-ARPES) to a multilayer C_{60} crystal evaporated onto Cu(111), where the film thickness was such that no photoemission signature of the underlying Cu(111) could be observed in our experiment. We verified the sample quality by performing momentum microscopy of the occupied HOMO and HOMO-1 states simultaneously to the measurement of the excited states (see Supplementary Fig. S1). Femtosecond exciton dynamics were induced using ≈ 100 fs, hv = 2.9 eV or ≈ 100 fs, hv = 3.6 eV laser pulses derived from the frequency-doubled output of a optical parametric amplifier. The exciton dynamics were probed using our custom photoemission momentum microscope with a 500 kHz ultrafast 26.5 eV extreme ultraviolet (EUV) light source[39] that enables us to map the photoelectron momentum distribution over the full photoemission horizon in a kinetic energy range exceeding 6 eV and an overall time resolution of ≈ 100 fs (the EUV pulse length is about 20 fs). The pump fluence was set to 90(10) µJ/cm² and 20(5) µJ/cm² for the hv = 2.9 eV and the hv = 3.6 eV measurement, respectively. In both cases, we found that p-polarized light excites the material most efficiently, leading to an excitation density on the order of 1 excitation per 1000 molecules. To prevent the free rotation of C_{60} molecules, we cooled the sample down to ≈ 80 K[43]. In addition to the resulting long-range periodic ordering of the C_{60} crystal, cooling was also observed to prevent light-induced polymerization.

Momentum microscopy data preprocessing

In the momentum microscopy experiment, a balance has to be found between sufficiently low pump and probe light intensities to avoid space-charge effects, but also having sufficient intensity for the optical excitation (pump) and reasonably short integration times (probe). For the present experiment, we estimate that the pump and probe pulses each induce less than 50 photoelectrons over the full ($\approx 200 \times 150$ µm²) footprint of the beam. A 40 µm diameter spatial selection aperture and a low threshold voltage then eliminate most of the low-energy photoelectrons and pass less than 1 photoelectron per pulse to the time-of-flight detector. For our settings, small space-charge effects are present in the data, but these do not lead to strong distortions in the band-structure data and can be easily corrected. Therefore, the first step in the data analysis was to subtract a space-charge-induced delay- and momentum-dependent kinetic energy shift which affects the full data set. For this purpose, the central kinetic energy of the HOMO was determined for normalization. To avoid the influence of the C_{60} crystal band structure[42], we fitted a two-dimensional Lorentzian[44] and shifted the kinetic energy distribution accordingly, leading to the expected overall flat shape of the molecular orbitals in the ARPES data.

Although we use narrow-band multilayer mirrors to select the 11th harmonic at hv = 26.5 eV from our laser-based high-harmonic generation spectrum[39], we observe subtle replicas of the HOMO, HOMO-1, and HOMO-2 states in the unoccupied regime of the spectrum that are caused by photoemission from the 13th harmonic at at hv = 31.2 eV. To quantify these replica signals, we fitted the static reference spectrum above $E - E_H > 1.2$ eV (i.e., in the unoccupied regime of the spectrum) with three Gaussian-shaped peaks for the HOMO replicas and an exponential function to account for residual photoemission intensity in the unoccupied regime that is caused in this spectral region by the much stronger direct 11th harmonic one-photon-photoemission from the HOMO state. After carrying out this fitting routine, we are able to calculate clean 11th harmonic spectra (static and time-resolved) via subtraction of the fitted 13th harmonic HOMO replicas. Note that we only subtract the replica signals, but not the background signal that is caused by one-photon-photoemission with the 11th harmonic from the HOMO state, because this background is time-dependent[24], and needs

Table 1 | Peak parameters for hv = 2.9 eV excitation, extracted using Eq. (3)

Exciton	Kin. Energy (eV)	Bandwidth (FWHM) (eV)
S_3 (t = 0 fs)	2.768(2)	0.606(4)
S_2	1.978(2)	0.406(3)
S_1	1.667(1)	0.362(2)

Note that we give the full width at half maximum (FWHM) for the bandwidth.

to be explicitly considered in the fitting procedure. The data shown in Fig. 3 of the main text is processed in the way described above.

Fitting procedure for the time-resolved data

From replica-free trPES data for hv = 2.9 eV excitation, we determine the amplitude A_i, kinetic energy E_i, and bandwidth ΔE_i for the ith exciton signature using a global fitting approach. In particular, we apply the model

$$I(E,t) = \frac{A_{S_3}(t)}{\sqrt{2\pi}\Delta E_{S_3}} \exp\left[(E - E_{S_3}(t))^2/\Delta E_{S_3}^2\right]$$
$$+ \frac{A_{S_2}(t)}{\sqrt{2\pi}\Delta E_{S_2}} \exp\left[(E - E_{S_2})^2/\Delta E_{S_2}^2\right]$$
$$+ \frac{A_{S_1}(t)}{\sqrt{2\pi}\Delta E_{S_1}} \exp\left[(E - E_{S_1})^2/\Delta E_{S_1}^2\right]$$
$$+ A_{bg}(t)\exp\left[-E/\tau\right]. \tag{3}$$

Here, the last term is needed to account for the above-mentioned delay-dependent photoemission intensity that is caused by a transient renormalization of the HOMO state, as found in ref. 24.

The fit results of this model applied to the hv = 2.9 eV excitation and momentum-integrated data are shown in Table 1, and Supplementary Fig. S2a for the time-resolved exciton dynamics.

For the measurement with hv = 3.6 eV excitation, we account for the S_4 exciton band by extending the model in Eq. (3) with a set of Gaussian peaks with identical temporal evolution, given by

$$I(E,t) = \ldots + \frac{A_{S_4}(t)}{2\sqrt{2\pi}\Delta E_{S_4}} \left(\exp\left[(E - E_{S_4,\text{upper}})^2/\Delta E_{S_4}^2\right] \right.$$
$$\left. + \exp\left[(E - E_{S_4,\text{lower}})^2/\Delta E_{S_4}^2\right] \right), \tag{4}$$

which follows the same notation as Eq. (3). Here, we set $E_{S_4,\text{upper}}$ to be close to 3.6 eV, and following the *GW*+BSE calculation we set $E_{S_4,\text{upper}} - E_{S_4,\text{lower}} = 1.4$ eV. Fitting this model to the momentum-integrated hv = 3.6 eV excitation data, we find $E_{S_4,\text{upper}} = 3.59(1)$ eV, and for the FWHM of the S_4 we find 0.58(3) eV. The time-resolved amplitudes retrieved using this model are shown in Supplementary Fig. S2b. Furthermore, this analysis was used in Fig. 3 of the main text to subtract the exponential background $A_{bg}(t)\exp\left[-E/\tau\right]$ related to the transient broadening of the HOMO state.

Fitting procedure for the time- and momentum-resolved data

In order to analyze the time-resolved data also momentum-resolved and thereby retrieve the momentum patterns that are shown in Fig. 4 in the main text, we carry out the fitting routine separately for pixel-resolved energy-distribution curves in the momentum distribution (1 pixel corresponds to ≈ 0.02 Å⁻²). Despite our efforts to reduce space charge, a residual noise signal remains near the center of the photoemission horizon, leading to a small region where the low signal-to-background ratio does not allow a reliable fit. We therefore exclude this region in our analysis (gray areas in Fig. 4 in the main text). Also, for the momentum-resolved data, the replica HOMO background

signals due to the 13th harmonic amounts to 0, 1 or at most 2 counts in the pixel-resolved (momentum-resolved) energy-distribution curves, and can therefore not be fitted and subtracted accurately as described above for the momentum-integrated data. As such, we need to ignore the HOMO replicas from the 13th harmonic in the momentum-resolved analysis. We avoid overfitting of the model in Eq. (3) by fixing the energy and bandwidth of the peaks in the fitting routine to the parameters given in Table 1. Thus, the set of free parameters in the momentum-resolved fitting procedure is limited to $A_{S3}(k)$, $A_{S2}(k)$, $A_{S1}(k)$ and $A_{bg}(k)$. This approach enables the extraction of reliable momentum distributions also for the partially overlapping energy distributions of the S_1 and S_2. The 1σ errors for the full momentum maps are shown in Supplementary Fig. S3.

We note that the overall photoemission intensity of the S_4 peak in the hv = 3.6 eV excitation data is comparably low due to the sub-50 fs decay to the lower-energy S_3 excitons (see Fig. 3 in main text and Supplementary Fig. S2b). Furthermore, with hv = 3.6 eV excitation, two-photon photoemission with 2 * 3.6 eV = 7.2 eV is sufficient to overcome the work function, so that space-charge effects could only be avoided by considerably reducing the hv = 3.6 eV pump intensity. Therefore, the signal-to-noise ratio in these measurements was not sufficient for a momentum-resolved analysis of the S_4 exciton data.

Calculation of the C_{60} exciton spectrum

The ab initio calculation of the exciton spectrum of the C_{60} film was performed in two steps, using a GW+BSE approach. For the static electronic structure, we perform calculations for two unique C_{60} dimers, which have been extracted from the known structure of the molecular film[45] (see Fig. 2c, dimers 1-2 and 1-4 respectively). Starting from Kohn-Sham orbitals and energies of a ground state DFT calculation (6-311G*/PBE0+D3)[46–49] using ORCA 5.0.1[50,51], we employ the Fiesta code[52] to self-consistently correct the molecular energy levels by quasi-particle self-energy calculations with the GW approximation. To account for polarization effects beyond the molecular dimer, we embed the dimer cluster in a discrete polarizable model using the MESCal program[53–55]. We found that mimicking 2 layers of the surrounding C_{60} film in such a way resulted in the convergence of the band gap within 0.1 eV with a removal energy from the highest valence level of 6.65 eV. The close agreement of this quasi-particle energy with the experimentally determined work function of 6.5 eV gives us additional confidence in the choice of our embedding environment. The calculated quasi-particle energy levels are shown in Fig. 2a. Here the finite width of the black bars actually arises from multiple energy levels forming bands on the energy axis. We characterize them according to symmetry[56] as HOMO-1, HOMO, LUMO, and LUMO+1 bands, each consisting of 18, 10, 6 and 6 energy levels per dimer, respectively. Note that the HOMO-1 is made up by states from two different irreducible representations of the isolated gas phase C_{60} molecule which are practically forming a single band.

Building upon the GW energies, we compute neutral electron-hole excitations by solving the Bethe-Salpeter equation beyond the Tamm-Dancoff approximation (TDA). This yields the excitation energies Ω_m and the electron-hole coupling coefficients $X_{vc}^{(m)}$ for a series of excitons labeled with m. We first analyze the resulting optical absorption spectrum which is shown in Fig. 2c as black solid line. It reveals a prominent absorption band around hv = 3.6 eV that is well-known from gas-phase spectroscopy[57]. Secondly, the dimer calculation reveals a strong optical absorption at hv = 2.8 eV as well as a weakly dipole-allowed transition at hv = 2 eV. Both of these transitions are known to only appear in aggregated phases of C_{60}[23], and cannot be understood by considering only a single C_{60} molecule. We refer to the exciton bands around $\Omega = 1.9$, 2.1, 2.8 and 3.6 eV as S_1, S_2, S_3 and S_4, respectively.

In line with our classification of the GW energy levels, one can group the composition of the excitons into four categories according

to the contributing quasi-particle energy levels. As visualized in Fig. 2c, this shows that S_1 and S_2 are almost completely described by HOMO to LUMO transitions. On the other hand, S_3 is predicted to have a small contribution of HOMO-1 character, however this contribution is too small to be reliably measured in our experiment. Finally, for S_4 we observe a clear and almost equal mixture of HOMO-1 and HOMO contributions, which is also confirmed by our measurements. Contributions from lower lying valence bands are negligibly small in the studied energy window.

Calculation of the exciton momentum maps

Based on our Kohn-Sham orbitals and BSE excitation coefficients, we calculate theoretical momentum maps for each exciton according to Eq. (2) following the derivation of Kern et al.[19]. Note that for better readability, Eqs. (1) and (2) are given within the TDA, however, can in general be extended to include also de-excitation terms[19]. In the present case, we found the de-excitation contributions to be marginal (below 1%) without affecting the appearance of the momentum maps and our interpretation. The energy conservation term comprises the BSE excitation energies (Ω_m), the GW quasi-particle energies for electron removal (i.e. ionization potential ε_v), and the probe energy of hv = 26.5 eV in accordance with our experimental setup. Furthermore, we include an inner potential to correct for the photoemission intensity variation of 3D molecules along the moment vector component perpendicular to the surface. Here, we choose a value of 12.5 eV, which has already been shown to match with experimental C_{60} data[42,58]. (Note that while considering the inner potential of the film is essential to describe the ARPES fingerprint, a variation of the inner potential between 12 and 14 eV indicated no influence on the interpretation of our results).

As we exploited the plane-wave approximation, the calculated photoemission intensity is modulated by the momentum-dependent polarization factor $|Ak|^2$, which we modeled as p-polarized light incoming with 68° to the surface normal according to experiments. To account for the symmetry of the C_{60} film, the momentum maps were 3-fold rotated and mirrored. Finally, application of Eq. (2) provides us with a 3D data set of simulated photoemission intensity as a function of the kinetic energy (E_{kin}) and the momentum components k_x and k_y for each individual exciton with excitation energy Ω_m. Analogous to experiment, we referenced the kinetic energy against the energy of the HOMO. The calculated ionization potential was further used to set the photoemission horizon of the theoretical momentum maps. Next, we estimate the population of the different excitonic states and sum up the corresponding 3D photoelectron intensity distributions. Here, we note that the experimental linewidth of the excitonic features is significantly broadened by various external factors, such as inhomogeneity in the sample and a finite energy resolution of the experiment. Therefore, we assume that the different excitonic states within each band are populated equally. For the S_1, this includes all excitons from 1.8–2.0 eV, for S_2 the 2.0–2.2 eV range, and for S_3 2.7–3.0 eV. Finally, to arrive at the theoretical momentum maps shown in Fig. 4, we integrate the total signal in a wide kinetic energy range centered on the respective exciton band.

Data availability

The data sets that support the experimental findings of this study are available on GRO.data with the identifier https://doi.org/10.25625/Q7TCIS[59]. The python codes to evaluate the theoretical data can be obtained from the authors upon request.

References

1. Zhu, X.-Y., Yang, Q. & Muntwiler, M. Charge-transfer excitons at organic semiconductor surfaces and interfaces. *Acc. Chem. Res.* **42**, 1779–1787 (2009).
2. Smith, M. B. & Michl, J. Singlet fission. *Chem. Rev.* **110**, 6891–6936 (2010).

3. Marongiu, D., Saba, M., Quochi, F., Mura, A. & Bongiovanni, G. The role of excitons in 3D and 2D lead halide perovskites. *J. Mater. Chem. C.* **7**, 12006–12018 (2019).

4. Mueller, T. & Malic, E. Exciton physics and device application of two-dimensional transition metal dichalcogenide semiconductors. *npj 2D Mater. Appl.* **2**, 1–12 (2018).

5. Chernikov, A. et al. Exciton binding energy and nonhydrogenic rydberg series in monolayer WS_2. *Phys. Rev. Lett.* **113**, 076802 (2014).

6. Pei, J., Yang, J., Yildirim, T., Zhang, H. & Lu, Y. Many-body complexes in 2D semiconductors. *Adv. Mater.* **31**, 1706945 (2019).

7. Zheng, X. & Zhang, X. *Advances in Condensed-Matter and Materials Physics: Rudimentary Research to Topical Technology*, 200 (eds. Thirumalai, J. & Ivanovich Pokutnyi, S.) (IntechOpen, 2020).

8. Rohlfing, M. & Louie, S. G. Electron-hole excitations and optical spectra from first-principles. *Phys. Rev. B* **62**, 4927 (2000).

9. Mitterreiter, E. et al. The role of chalcogen vacancies for atomic defect emission in MoS_2. *Nat. Commun.* **12**, 3822 (2021).

10. Martin, R. L. Natural transition orbitals. *J. Chem. Phys.* **118**, 4775–4777 (2003).

11. Krylov, A. I. From orbitals to observables and back. *J. Chem. Phys.* **153**, 080901 (2020).

12. Puschnig, P. et al. Reconstruction of molecular orbital densities from photoemission data. *Science* **326**, 702–706 (2009).

13. Jansen, M. et al. Efficient orbital imaging based on ultrafast momentum microscopy and sparsity-driven phase retrieval. *N. J. Phys.* **22**, 063012 (2020).

14. Wallauer, R. et al. Tracing orbital images on ultrafast time scales. *Science* **371**, 1056–1059 (2021).

15. Neef, A. et al. Orbital-resolved observation of singlet fission. *Nature* **616**, 275–279 (2023).

16. Karni, O. et al. Structure of the moiré exciton captured by imaging its electron and hole. *Nature* **603**, 247–252 (2022).

17. Schmitt, D. et al. Formation of moiré interlayer excitons in space and time. *Nature* **608**, 499–503 (2022).

18. Dong, S. et al. Direct measurement of key exciton properties: energy, dynamics and spatial distribution of the wave function. *Nat. Sci.* **1**, e10010 (2021).

19. Kern, C. S., Windischbacher, A. & Puschnig, P. Photoemission orbital tomography for excitons in organic molecules. *Phys. Rev. B* **108**, 085132 (2023).

20. Ke, W. et al. Efficient planar perovskite solar cells using room-temperature vacuum-processed C_{60} electron selective layers. *J. Mater. Chem. A* **3**, 17971–17976 (2015).

21. Puente Santiago, A. R. et al. Tailoring the Interfacial Interactions of van der Waals 1T-MoS2/C60 heterostructures for high-performance hydrogen evolution reaction electrocatalysis. *J. Am. Chem. Soc.* **142**, 17923–17927 (2020).

22. Yu, Z. et al. Simplified interconnection structure based on C_{60}/SnO_{2-x} for all-perovskite tandem solar cells. *Nat. Energy* **5**, 657–665 (2020).

23. Wang, Y. M., Kamat, P. V. & Patterson, L. K. Aggregates of fullerene C_{60} and C_{70} formed at the gas-water interface and in DMSO/water mixed solvents. a spectral study. *J. Phys. Chem.* **97**, 8793–8797 (1993).

24. Stadtmüller, B. et al. Strong modification of the transport level alignment in organic materials after optical excitation. *Nat. Commun.* **10**, 1470 (2019).

25. Emmerich, S. et al. Ultrafast charge-transfer exciton dynamics in C_{60} thin films. *J. Phys. Chem. C* **124**, 23579–23587 (2020).

26. Hess, B. C., Bowersox, D. V., Mardirosian, S. H. & Unterberger, L. D. Electroabsorption in C_{60} and C_{70}. third-order nonlinearity in molecular and solid states. *Chem. Phys. Lett.* **248**, 141–146 (1996).

27. Causa', M., Ramirez, I., Martinez Hardigree, J. F., Riede, M. & Banerji, N. Femtosecond dynamics of photoexcited C_{60} Films. *J. Phys. Chem. Lett.* **9**, 1885–1892 (2018).

28. Hahn, T. et al. Role of intrinsic photogeneration in single layer and bilayer solar cells with C_{60} and PCBM. *J. Phys. Chem. C* **120**, 25083–25091 (2016).

29. Mumthaz Muhammed, M., Habeeb Mokkath, J. & J. Chamkha, A. Impact of packing arrangement on the optical properties of C_{60} cluster aggregates. *Phys. Chem. Chem. Phys.* **24**, 5946–5955 (2022).

30. Habeeb Mokkath, J. Delocalized exciton formation in C_{60} linear molecular aggregates. *Phys. Chem. Chem. Phys.* **23**, 21901–21912 (2021).

31. Kobayashi, H., Hattori, S., Shirasawa, R. & Tomiya, S. Wannier-Like delocalized exciton generation in C_{60} fullerene clusters: a density functional theory study. *J. Phys. Chem. C* **124**, 2379–2387 (2020).

32. Blase, X., Duchemin, I., Jacquemin, D. & Loos, P.-F. The bethe-salpeter equation formalism: from physics to chemistry. *J. Phys. Chem. Lett.* **11**, 7371–7382 (2020).

33. Sun, H. & Autschbach, J. Electronic energy gaps for π-conjugated oligomers and polymers calculated with density functional theory. *J. Chem. Theory Comput.* **10**, 1035–1047 (2014).

34. Cocchi, C. & Draxl, C. Optical spectra from molecules to crystals: insight from many-body perturbation theory. *Phys. Rev. B.* **92**, 205126 (2015).

35. Weinelt, M., Kutschera, M., Fauster, T. & Rohlfing, M. Dynamics of exciton formation at the Si(100) c(4 × 2) surface. *Phys. Rev. Lett.* **92**, 126801 (2004).

36. Zhu, X. Y. How to draw energy level diagrams in excitonic solar cells. *J. Phys. Chem. Lett.* **5**, 2283–2288 (2014).

37. Kunin, A. et al. Momentum-resolved exciton coupling and valley polarization dynamics in monolayer WS_2. *Phys. Rev. Lett.* **130**, 046202 (2023).

38. Medjanik, K. et al. Direct 3D mapping of the Fermi surface and Fermi velocity. *Nat. Mater.* **16**, 615–621 (2017).

39. Keunecke, M. et al. Time-resolved momentum microscopy with a 1 MHz high-harmonic extreme ultraviolet beamline. *Rev. Sci. Instrum.* **91**, 063905 (2020).

40. Wallauer, R. et al. Momentum-resolved observation of exciton formation dynamics in monolayer WS_2. *Nano Lett.* **21**, 5867–5873 (2021).

41. Madéo, J. et al. Directly visualizing the momentum-forbidden dark excitons and their dynamics in atomically thin semiconductors. *Science* **370**, 1199–1204 (2020).

42. Haag, N. et al. Signatures of an atomic crystal in the band structure of a C_{60} thin film. *Phys. Rev. B* **101**, 165422 (2020).

43. Wang, H. et al. Orientational configurations of the C_{60} molecules in the (2 × 2) superlattice on a solid C_{60} (111) surface at low temperature. *Phys. Rev. B* **63**, 085417 (2001).

44. Schönhense, B. et al. Multidimensional photoemission spectroscopy—the space-charge limit. *N. J. Phys.* **20**, 033004 (2018).

45. David, W. I. F., Ibberson, R. M., Dennis, T. J. S., Hare, J. P. & Prassides, K. Structural phase transitions in the fullerene C_{60}. *Europhys. Lett.* **18**, 219 (1992).

46. Krishnan, R., Binkley, J. S., Seeger, R. & Pople, J. A. Self-consistent molecular orbital methods. xx. a basis set for correlated wave functions. *J. Chem. Phys.* **72**, 650–654 (1980).

47. Frisch, M. J., Pople, J. A. & Binkley, J. S. Self-consistent molecular orbital methods 25 supplementary functions for gaussian basis sets. *J. Chem. Phys.* **80**, 3265–3269 (1984).

48. Adamo, C. & Barone, V. Toward reliable density functional methods without adjustable parameters: The PBE0 model. *J. Chem. Phys.* **110**, 6158–6170 (1999).

49. Grimme, S., Antony, J., Ehrlich, S. & Krieg, H. A consistent and accurate ab initio parametrization of density functional dispersion correction (DFT-D) for the 94 elements H-Pu. *J. Chem. Phys.* **132**, 154104 (2010).

50. Neese, F. The ORCA program system. *Wiley Interdiscip. Rev. Comput. Mol. Sci.* **2**, 73–78 (2012).

51. Neese, F. Software update: the ORCA program system—Version 5.0. *WIREs Comput. Mol. Sci.* **12**, e1606 (2022).

52. Jacquemin, D., Duchemin, I. & Blase, X. Is the bethe–salpeter formalism accurate for excitation energies comparisons with TD-DFT, CASPT2, and EOM-CCSD. *J. Phys. Chem. Lett.* **8**, 1524–1529 (2017).

53. D'Avino, G., Muccioli, L., Zannoni, C., Beljonne, D. & Soos, Z. G. Electronic polarization in organic crystals: a comparative study of induced dipoles and intramolecular charge redistribution schemes. *J. Chem. Theory Comput.* **10**, 4959–4971 (2014).

54. Li, J., D'Avino, G., Duchemin, I., Beljonne, D. & Blase, X. Combining the many-body GW formalism with classical polarizable models: insights on the electronic structure of molecular solids. *J. Phys. Chem. Lett.* **7**, 2814–2820 (2016).

55. Li, J. et al. Correlated electron-hole mechanism for molecular doping in organic semiconductors. *Phys. Rev. Mater.* **1**, 025602 (2017).

56. Dresselhaus, M., Dresselhaus, G. & Eklund, P. *Science of Fullerenes and Carbon Nanotubes* (eds Dresselhaus, M., Dresselhaus, G. & Eklund, P.) 413–463 (Academic Press, San Diego, 1996).

57. Dai, S., Mac Toth, L., Del Cul, G. D. & Metcalf, D. H. Ultraviolet-visible absorption spectrum of C_{60} vapor and determination of the C_{60} vaporization enthalpy. *J. Chem. Phys.* **101**, 4470–4471 (1994).

58. Hasegawa, S. et al. Origin of the photoemission intensity oscillation of C_{60}. *Phys. Rev. B.* **58**, 4927–4933 (1998).

59. Bennecke, W. et al. Replication data for: Disentangling the multi-orbital contributions of excitons by photoemission exciton tomography. https://doi.org/10.25625/Q7TCIS, GRO.Data, (2024).

Acknowledgements

Author contributions

D.St., M.R., S.S., M.A., B.S., P.P., G.S.M.J. and S.M. conceived the research. W.B., D.Sc. and J.P.B. carried out the time-resolved momentum microscopy experiments. W.B. analyzed the data. W.B. and R.H. prepared the samples. A.W., C.S.K., G.D, X.B. and P.P. performed the calculations and analyzed the theoretical results. All authors discussed the results. G.S.M.J. and S.M. were responsible for the overall project direction and wrote the manuscript with contributions from all co-authors.

Funding

Competing interests

The authors declare no competing interests.

Additional information

Supplementary information The online version contains supplementary material available at https://doi.org/10.1038/s41467-024-45973-x.

Correspondence and requests for materials should be addressed to G. S. Matthijs Jansen or Stefan Mathias.

Peer review information *Nature Communications* thanks the anonymous reviewers for their contribution to the peer review of this work. A peer review file is available.

Reprints and permissions information is available at http://www.nature.com/reprints

Publisher's note Springer Nature remains neutral with regard to jurisdictional claims in published maps and institutional affiliations.